Article:
Chaves, V., Balbín, J.A., Navarro, A. et al. (2 more authors) (2023) Calculations of biaxial fatigue limits with models using the experimental crack direction. International Journal of Fatigue, 174. 107726. ISSN 0142-1123

https://doi.org/10.1016/j.ijfatigue.2023.107726

International Journal of Fatigue 174 (2023) 107726

Contents lists available at ScienceDirect

International Journal of Fatigue

journal homepage: www.elsevier.com/locate/ijfatigue

Calculations of biaxial fatigue limits with models using the experimental crack direction

V. Chaves [a,*], J.A. Balbín [a,b], A. Navarro [a], L. Susmel [c], D. Taylor [d]

[a] Departamento de Ingeniería Mecánica y Fabricación, Escuela Técnica Superior de Ingeniería, Universidad de Sevilla, Camino de los Descubrimientos s/n, 41092 Sevilla, Spain
[b] Departamento de Ingeniería Minera, Mecánica, Energética y de la Construcción, Escuela Técnica Superior de Ingeniería, Universidad de Huelva, Campus Universitario de El Carmen, 21007 Huelva, Spain
[c] Department of Civil and Structural Engineering, The University of Sheffield, Mappin Street, Sheffield S1 3JD, United Kingdom
[d] Department of Mechanical Engineering, Trinity College, Dublin 2, Ireland

ARTICLE INFO

Keywords:
Multiaxial fatigue
Notch
Fatigue limit
Crack path
Biaxial cyclic loading

ABSTRACT

Several models from the literature were used to predict the fatigue limit in notched components subjected to biaxial cyclic loading. The predictions of these models are based on the elastic stresses along a line which is considered to be representative of the crack direction in its initial part. The line used in the models changes considerably. For one of the studied models, the line direction corresponds to Mode I, while for another it is Mode II, and for the other two models considered the direction is between Mode I and Mode II. However, quite naturally, the experimental crack direction is unique. In recent years, a study of experimental fatigue limits and crack directions in its initial part for three materials was carried out in hollow cylindrical specimens with a circular hole subjected to cyclic axial, torsional and in-phase biaxial loading. The directions of the cracks that were measured experimentally are on average similar for the three materials and close to Mode I. The analysed models give, in general, good predictions of the experimental fatigue limits, although they use directions that are completely different and that they too differ markedly from the experimentally found ones. The predictions of the models using, in a forced way, the measured experimental directions are good in most cases, which reveals a surprising insensitivity of these models to the main hypotheses on which their own formulations are based.

1. Introduction

Fatigue failure in real components generally occurs at stress concentrations, commonly referred to as notches. There are various models in the literature to predict the fatigue limit in notched components subjected to cyclic multiaxial loading. Three of them are analyzed in this document. Two of these models [1,2] combine the Critical Plane Approach for unnotched solids under multiaxial loading with Taylor's Theory of Critical Distances (TCD) for notches under axial loading [3]. The third model is a short crack model that analyzes the interaction of the crack with the microstructural barriers of the material in the presence of a notch [4]. In the analysed models, the predictions are made based on the elastic stresses along a line whose length is of the order of the El Haddad small crack parameter, a_0 [5]. This line used in the models is considered representative of the experimental crack direction in its initial part. In the analyzed models, the direction of the line used varies considerably from one model to another: the Mode I direction, the Mode II direction and a mixed direction between that of Mode I and Mode II, depending on the type of material. Therefore, a great diversity of directions is used even though, evidently, the experimental crack direction is unique for a given geometry, loading and material. This diversity of directions used in the models might be due to the lack of a comprehensive experimental database on the direction of fatigue cracks growing from a notch for common industrial materials, especially in its initial part.

There are several investigations in the literature on the matter, such as the classical investigations by Fenner et al. on mild-steel specimens containing sharp V-grooves under alternating axial loading [6], by Frost on non-propagating cracks from sharp V-notches in cylindrical specimens under reversed axial and rotating bending loading for mild steel and aluminum alloy [7] and by Kitagawa and Takahashi on very small surface notches under uniaxial cyclic loading [8]. More recently, Endo's

* Corresponding author.
E-mail address: chavesrv@us.es (V. Chaves).

https://doi.org/10.1016/j.ijfatigue.2023.107726
Received 6 March 2023; Received in revised form 19 April 2023; Accepted 15 May 2023
Available online 22 May 2023

research on specimens containing small surface defects subjected to combined stress loading [9], Susmel and Taylor's work on sharply notched specimens under in-phase Mode I and II loading [10], Meneghetti et al.'s study on U-notch steel specimens under axial loading [11], Tanaka et al.'s study on steel specimens with a hole subject to in-phase and out-of-phase axial and torsional loadings [12], Berto et al.'s tests on V-notched specimens made of hardened and tempered steel [13], Gates and Fatemi's research on aluminum specimens with a circular hole subject to multiaxial loading [14], and Lorenzino and Navarro's tests on aluminum alloy plates with a circular hole under axial loading [15]. All these experimental results from the literature present a great diversity of directions of the initial part of the crack, so that it would be very difficult to establish a clear criterion to define the crack direction in its initial part for a given material, load and notch geometry.

In recent years, a comprehensive study of the experimental fatigue limits and crack directions in the initial part was carried out in hollow cylindrical specimens with a circular hole subjected to cyclic axial, torsional and in-phase biaxial loading. Three materials were tested, a stainless steel [16], a carbon steel [17] and an aluminum alloy [18]. All the details about the materials and the tests can be consulted in these previous documents [16–18]. These materials can be considered as brittle, intermediate ductile-brittle and ductile in fatigue, respectively, as will be seen later, which allows this study to analyze the effect of various material fatigue behaviors in the crack direction. The experimental crack directions were measured only for the broken specimens subjected to fatigue at a high number of cycles, with a life above 10^5 cycles. The present document shows an analysis of the measured experimental results. The fatigue limits predictions for the studied notches with the three multiaxial fatigue models for notches are also shown, and the average experimental crack directions are compared with the directions of the lines used by the models. As far as the authors are concerned, the exhaustive analysis of experimental crack directions for several materials from notches and the analysis of the models' predictions from two points of view, the numerical fatigue limit prediction and the direction of the crack used in the models, are novelties in our scientific field. In addition, the models' predictions using, in a forced way, as the line for the prediction the average experimental direction measured for each case are shown, constituting the second main novelty of this work. The objective is to analyze the adaptation capacity of each one of the models to the use of the experimental direction to make the predictions, which could be highly desirable in the near future, trusting that there will be a wide database of experimental cracks directions for notch multiaxial fatigue.

2. Materials and tests

The three materials analyzed in this work are commercial AISI 304L stainless steel, S355 low carbon steel and 7075-T6 aluminum alloy. The main mechanical properties of the three materials are shown in Table 1, which are as follows: tensile strength σ_{UTS}, yield strength σ_{YS}, axial and torsion fatigue limits, σ_{FL} and τ_{FL} (for $R_\sigma = -1$), average grain size d and El Haddad short-crack parameter $a_0 = (1/\pi)(\Delta K_{th}/\Delta\sigma_{FL})^2$ [5], where ΔK_{th} is the threshold value of ΔK for fatigue crack growth and $\Delta\sigma_{FL}$ the fatigue limit range. In the case of aluminum alloy, the values of σ_{FL} and τ_{FL} correspond to an estimated life of one million cycles, as aluminum does not have a defined fatigue limit. The ratio of the fatigue limits τ_{FL}/σ_{FL} is also shown. This ratio has been used by several authors as an indicator of ductility in fatigue, suggesting that ductile materials in fatigue have a value close to 0.5 and brittle materials a value close to 1 [19,20]. In this case, the values of the ratio are 0.91, 0.76 and 0.58 for AISI 304L, S355 and 7075-T6, respectively. Thus, AISI 304L can be considered as a brittle material in fatigue, 7075-T6 as a ductile material in fatigue (with a value of a von Mises type material), and S355 as a material with an intermediate ductile-brittle behavior in fatigue. The chemical composition and other properties of these materials can be consulted in [16,17] and [18].

The geometry of the notched specimen was a thin-walled tube of 1.5 mm thickness with a passing-through hole in the central section. Several hole radii R were studied, ranging from 0.4 to 1.7 mm. Fig. 1 shows the geometry of the specimen, in particular, the one with the hole radius $R = 0.5$ mm (1 mm diameter).

Three types of tests were performed with the notched specimens, in all cases under fully-reversed loading: axial tests, torsion test and in-phase axial-torsion tests, of the type $\sigma = \tau$, where σ is the normal stress amplitude and τ is the maximum shear stress amplitude, at the transverse cross-section, calculated with the equations of elasticity. The axial tests were made in a resonance machine, at a frequency of 100–150 Hz, and the torsional and biaxial tests in a servo-hydraulic axial-torsion load frame, at 6–10 Hz. The tests were stopped when a long crack of at least several mm was obtained or when a certain number of cycles were reached (run-outs). For AISI 304L stainless steel, the run-out was established at 3.5×10^6 cycles, for S355 steel at 5×10^6 cycles and for 7075-T6 aluminum at 50×10^6 cycles for axial tests and at 5×10^6 cycles for torsion and biaxial tests.

3. Fatigue limits of the notched specimens

The results of the fatigue tests of the notched specimens were used to construct the S-N curves and calculate the fatigue limits. Table 2 shows the experimental fatigue limits, expressed in term of stress amplitude, of the notched specimens, σ_{FL}^N and τ_{FL}^N, including the three materials, various hole radii R and the three types of loading, with a total of 15 values. For aluminum, the fatigue resistance values corresponding to one million cycles were taken again. Table 2 also includes the fatigue limit predictions with the models, which will be explained later in the document.

4. Experimental crack directions

This section shows the experimental values of the crack initiation location and the crack direction in its initial part, both measured on the outer surface of the specimen. As mentioned in the introduction, it is important to determine the experimental crack direction in its initial part, since the most common models to calculate the fatigue limit in notches base their prediction on the elastic stresses in a line that is representative of the crack direction in this phase. Only specimens that failed after 10^5 cycles, within the so-called high cycle fatigue regime were considered. For the three materials all the cracks originated from the circular hole, and on both sides of the hole, as expected, since the hole is a stress concentrator. Fig. 2(a) shows the coordinate system $OXYZ$ to define the crack direction, with its origin O located at the center of the circular hole on the outer surface of the specimen. The X-axis is in the central transverse section of the specimen, the Y-axis runs along the longitudinal dimension of the specimen and the Z-axis coincides with

Table 1
Properties of the studied materials.

Material	σ_{UTS}(MPa)	σ_{YS}(MPa)	σ_{FL}(MPa)	τ_{FL}(MPa)	τ_{FL}/σ_{FL}	d, grain size (mm)	a_0 (mm)
AISI 304L stainless steel [16]	654	467	316	288	0.91	0.080	0.180
S355 low carbon steel [17]	586	412	275	208	0.76	0.033	0.158 [(a)]
7075-T6 aluminum alloy [18]	657	595	258	149	0.58	0.015	0.072 [(a)]

(a) Estimated as $a_0 = 3.1^2 d/2$ (see [21]).

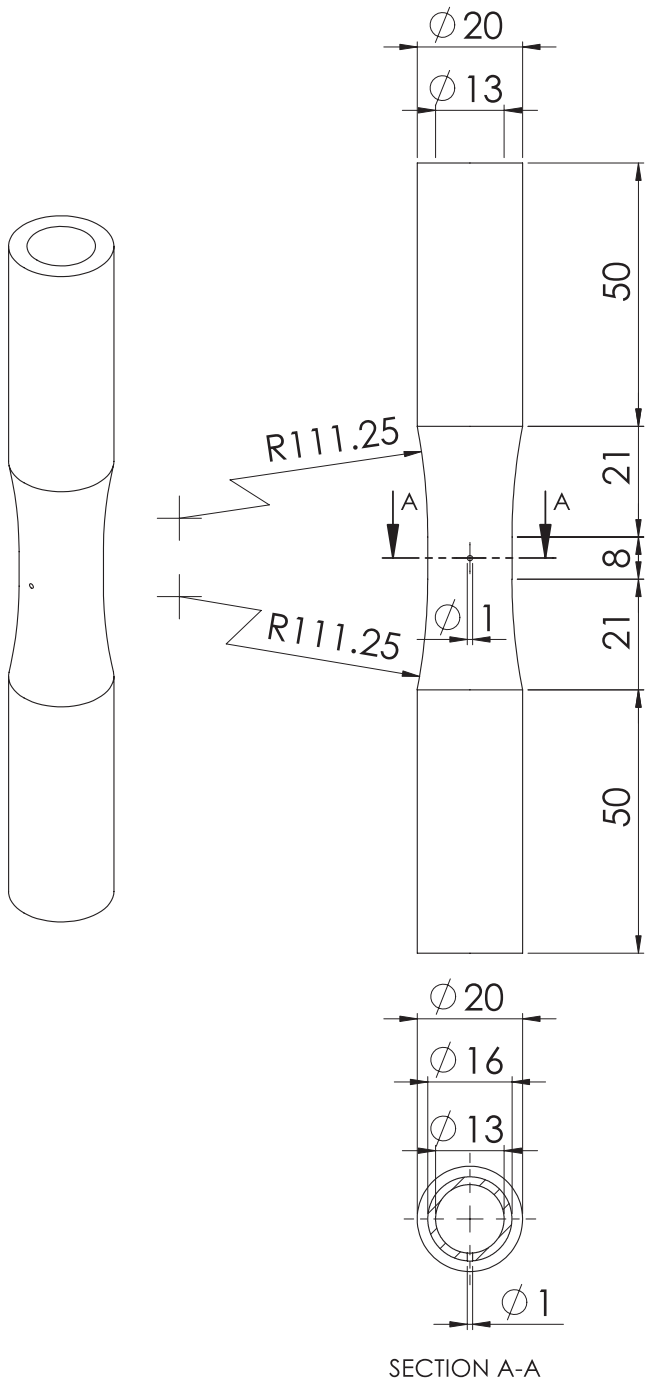

Fig. 1. Geometry of the notched specimen.

the axis of the hole. The location of the crack initiation point at the hole contour and the crack direction for a certain crack length $a = \sqrt{(\Delta x')^2 + (\Delta y')^2}$ are indicated by the angles θ and θ_1, respectively, whose geometrical definition are sketched in Fig. 2(b). Angles are measured counterclockwise. The crack initiation point angle θ is defined as $\tan^{-1}(\Delta Y/\Delta X)$. The crack direction angle θ_1 is measured using an additional coordinate system $o'x'y'$ whose origin coincides with the crack initiation point at the hole contour. The angle θ_1 is defined as $\tan^{-1}(\Delta y'/\Delta x')$. This crack direction angle θ_1 was measured experimentally for a crack length a equal to 0.50, 0.08 and 0.15 mm for the AISI 304L, S355 and 7075-T6 specimens, respectively. These crack length values are equal in length to $2.8a_0$, $0.5a_0$, and $2.1a_0$, respectively, or expressed as a function of average grain size, equal to $6.2d$, $2.4d$, and $10d$, respectively. These values, of the order of magnitude of a_0, were considered representative of the crack direction in its initial part. As will be seen later in the description of the models, they use a line whose length is of this order of magnitude to make the predictions. The choice of these lengths will be justified in the discussion section.

The methodology used for measuring the crack initiation location and the crack direction angles is as follows:

- The diameter of the circular hole is measured before the fatigue tests is carried out.
- Once the fatigue test is complete, a high-quality picture of the hole with the crack is taken with an optical microscope. Before taking the picture, the specimen is carefully placed longitudinally under the microscope so that the y-axis of the picture coincides with the longitudinal axis of the specimen. On this picture, displayed on a large computer screen, the angles will be measured.
- The presence of the crack divides the circular hole into two halves. One of the hole halves and its adjacent crack lines are selected for the measurements.
- A circumference is drawn on the picture with a diameter equal to the diameter of the hole measured before the test. This circumference is made to coincide with the chosen half of the circular hole. The center of this circumference provides the center of the circular hole (origin of the $OXYZ$ coordinate system defined in Fig. 2). The horizontal and vertical axes of the picture will be the X and Y axes of the coordinate system, respectively. Then, the OXY coordinate system is established in the picture.
- The crack initiation point at the edge of the hole half is located and the crack initiation location angle θ is measured.
- The additional coordinate system $o'x'y'$ is defined at the crack initiation point.
- From the origin o', an arc of radius a is drawn. Its intersection with the crack line defines a point. The line that joins this point with the origin o' provides the angle θ_1.

A limitation of this measurement methodology is that the crack angle is defined by just two points and a straight line, so the possible zig-zagging of the crack path between these two points is not taken into account.

Fig. 3, Fig. 4 and Fig. 5 show representative pictures of the experimental cracks for the AISI 304L, S355 and 7075-T6, respectively. The calculated crack angles are also shown. Please note that for the sake of clarity the circumferences were not drawn in these pictures. For material S355 there are only axial tests. For this material, an enlarged picture of the left crack and another of the right crack have been added (Fig. 4(b) and Fig. 4(c)), since the angle θ_1 could not be clearly observed in the general picture (Fig. 4(a)), due to the fact that this material crack length a is very small. A tortuous crack path in these initial zones of the two cracks is observed. In some torsional tests, such as the one in Fig. 3(b), four cracks were observed. In this work only the two main cracks were analyzed. Table 3 shows a summary of the averages experimental crack angles θ and θ_1 for the studied materials, loading and hole radii. In addition, standard deviation values are included in parentheses. In total, the angles of 106 specimens were measured, 37 of AISI 304L, 22 of S355 and 47 of 7075-T6. Table 3 also includes the crack lines angles θ and θ_1 used by the models to make the predictions, which will be explained later in the document. For the three materials, on average, the experimental crack initiation point is close to the point of maximum principal stress at the hole contour, i.e. $\theta = 0^\circ$ for axial load, $\theta = 45^\circ$ for torsional load and $\theta = 31.7^\circ$ for biaxial load. The experimental crack direction in its initial part, measured for a crack length a, is, for the three materials, on average, close to the direction of maximum principal stress, i.e. $\theta_1 = 0^\circ$ for axial load, $\theta_1 = 45^\circ$ for torsional load and $\theta_1 = 31.7^\circ$ for biaxial load. An effect of the type of material in the average crack initiation point and crack direction was not appreciated.

Table 2
Experimental fatigue limits of the notched specimens and model's predictions.

Material	R, hole radius (mm)	Type of loading	Notch fatigue limit, σ_{FL}^N or τ_{FL}^N (MPa)				
			Experimental	Model's predictions			
				MWCM+PM (Mode I)	MWCM+PM (Mode II)	Carpinteri et al.	Biaxial N-R
AISI 304L	0.5	Axial	148	125.6	124.7	149.1	145.0
	1	Axial	154	118.4	116.0	128.6	118.7
	1.5	Axial	151	114.7	112.6	121.5	110.3
	0.5	Torsion	133	107.9	104.1	124.5	124.6
	1	Torsion	130	94.5	91.2	102.1	96.0
	0.5	Biaxial ($\sigma = \tau$)	117	73.1	71.5	85.7	84.5
S355	0.4	Axial	175	127.2	121.8	134.1	142.4
	0.75	Axial	152	112.4	107.8	117.2	117.9
	1.7	Axial	138	101.2	98.7	105.8	102.4
7075-T6	0.5	Axial	95	105.1	100.1	96.6	119.6
	1	Axial	94	95.5	92.8	91.2	110.0
	1.5	Axial	85	92.3	90.5	89.5	107.3
	0.5	Torsion	75	82.5	77.7	74.9	94.5
	1	Torsion	67	73.3	70.8	69.6	83.8
	0.5	Biaxial ($\sigma = \tau$)	65	58.8	55.7	53.7	66.6
Average error (%)				**17.5 %**	**18.1 %**	**12.1 %**	**18.7 %**

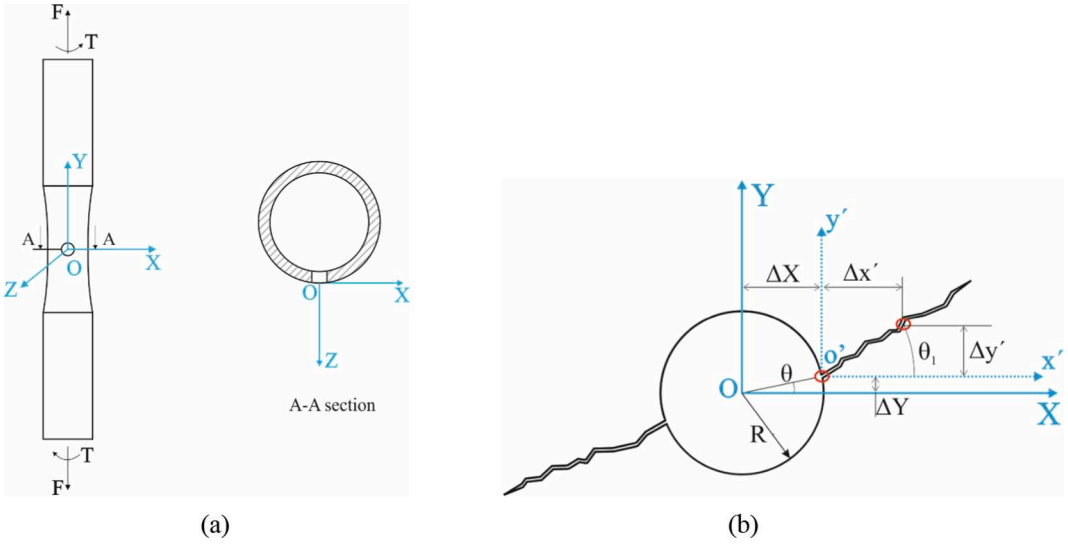

Fig. 2. (a) Sketch of the specimen with the axes. (b) Detail of the hole with the cracks and the variables used to define the crack direction.

5. Brief description of three biaxial fatigue models for notches

In this section a brief description of the following three multiaxial notch fatigue models is presented: the combined model of Susmel and Taylor (MWCM+PM), the combined model of Carpinteri et al. and the biaxial Navarro-Rios model.

5.1. The combined model of Susmel and Taylor (MWCM+PM)

It consists of combining the Critical Plane Approach proposed by Susmel for solids without notches under multiaxial loading, called the Modified Whöler Curve Method (MWCM) [1], with Taylor's Critical Distance Theory (TCD) for notches under axial loading [3]. The combined model consists of locating the point of maximum principal stress at the notch contour (the hot-spot). A straight line is then drawn from that point, representing the crack direction. There are two variants of the model: the Mode I variant, in which the line is drawn perpendicular to the notch contour at the hot-spot [22]; and the Mode II variant, in which the line is drawn at 45° with respect to the line of the Mode I variant [23]. It is worth remembering also that, for the Mode I variant, the focus path is suggested as being taken coincident with the notch bisector when stress concentrators are modelled by imposing that the notch root radius equals zero. Within the TCD, if the point method *PM* is chosen, then the point to make the prediction is located at the chosen line and at a distance of $a_0/2$ from the hot-spot. At this point, the critical plane is calculated as the one with the greatest value of the shear stress amplitude τ_a. The stress normal to that plane at the chosen point is called $\sigma_{n,max}$. From these two stresses, the fatigue limit of the notched component is reached if the following criterion is met:

$$\tau_a + \left(\tau_{FL} - \frac{\sigma_{FL}}{2}\right) \frac{\sigma_{n,max}}{\tau_a} = \tau_{FL} \tag{1}$$

Fig. 6(a) shows a sketch of the crack lines used for the MWCM+PM model for its two variants. The case of a plate with a hole under biaxial loading ($\sigma_y^\infty, \tau^\infty$) is represented. It is also shown the crack line used in the Carpinteri et al. model, which will be described below.

5.2. The combined model of Carpinteri et al.

This model is qualitatively similar to the previous one. The prediction is based on the stresses at a point located at $a_0/2$ from the hot-spot. In this case, the line where this point is located depends on the material and is defined by the angle δ with respect to the line normal to the notch contour at the hot-spot. The value of δ is calculated by the following

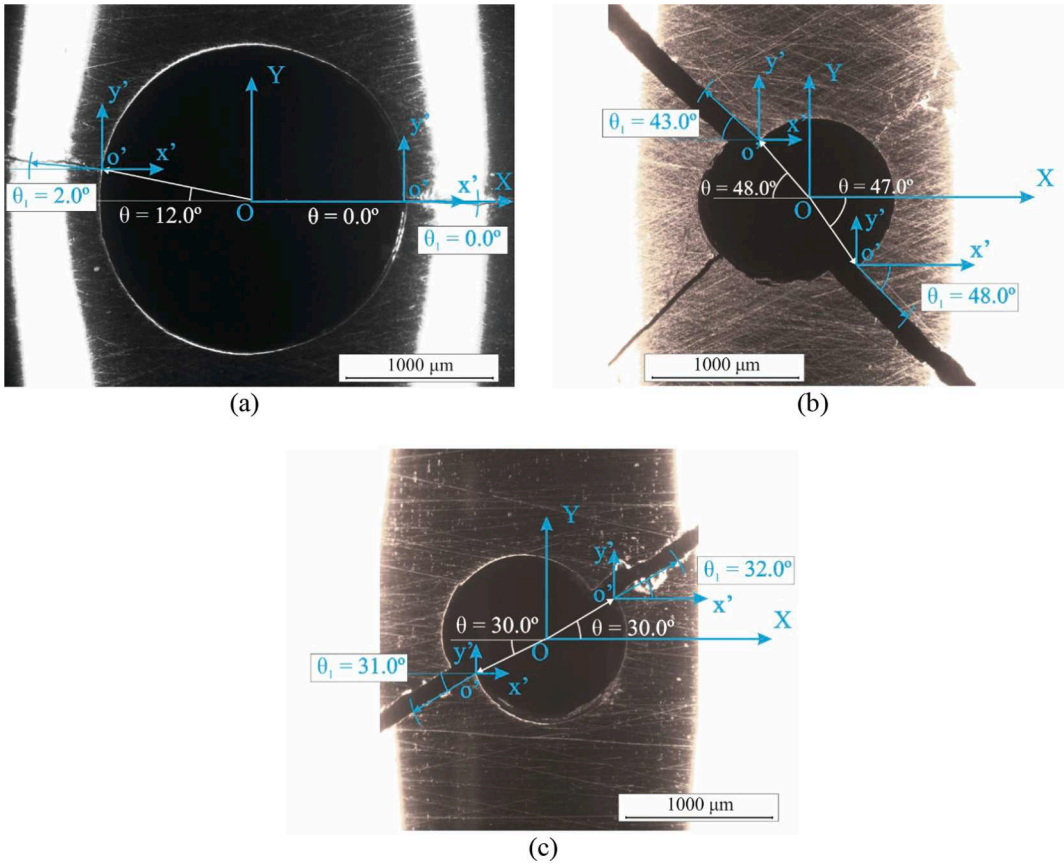

Fig. 3. Examples of experimental crack angles for AISI 304L: (a) Axial loading, R = 1 mm, σ = 200 MPa, N = 320,500 cycles. (b) Torsional loading, R = 0.5 mm, τ = 156 MPa, N = 385,700 cycles. (c) Biaxial loading, R = 1 mm, σ = τ = 130 MPa, N = 178,400 cycles.

equation [2]:

$$\delta = \frac{3\pi}{8}\left[1 - \left(\frac{\tau_{FL}}{\sigma_{FL}}\right)^2\right] \tag{2}$$

For materials with brittle behavior in fatigue, i.e. $\tau_{FL}/\sigma_{FL} = 1$, the line will coincide with that of the Mode I variant of the previous model, and for materials with ductile behavior in fatigue, with a value $\tau_{FL}/\sigma_{FL} = 0.58$, the line will coincide with that of the Mode II variant. Next, the normal stress N and shear stress C to the line at the critical point are calculated. An equivalent stress $\sigma_{eq,a}$ and the fatigue limit are defined by the following criterion:

$$\sigma_{eq,a} = \sqrt{N^2 + \left(\frac{\sigma_{FL}}{\tau_{FL}}\right)^2 C^2} = \sigma_{FL} \tag{3}$$

5.3. Biaxial Navarro-Rios model (biaxial N-R model)

The Navarro and de los Rios model (N-R model) [24,25] is a microstructural model that analyses the interaction of the crack and its associated plastic zone with microstructural barriers, such as grain boundaries. Mathematically, the crack, its plastic zone, and the microstructural barrier are modelled as a straight line by a distribution of dislocations. The remote applied stress necessary for the crack to overcome the successive barriers is calculated, the maximum of these values being the fatigue limit of the notched component. The equation to calculate the remote stress to overcome the i-th barrier, located at a distance of i grains from the crack initiation point, is the following [4]:

$$\frac{\sigma_3^i}{m_{\sigma i}^* \cdot \tau_c} + \frac{\tau_3^i}{m_{\tau i}^* \cdot \tau_c} = 1 \tag{4}$$

The stresses σ_3^i and τ_3^i represent the shear and normal stresses in the i-th barrier, calculated from the equilibrium of dislocations in the crack line, for the specific notched geometry and applied loads. The parameters $m_{\sigma i}^* \cdot \tau_c$ and $m_{\tau i}^* \cdot \tau_c$ represent the normal and tangential stresses required to overcome the i-th barrier and are adjusted for each material, based on the axial and torsional fatigue limits, σ_{FL} and τ_{FL}, and the Kitagawa-Takahashi diagram of the material. A characteristic of this model is that the crack line is not established a priori, as in previous models, but is calculated as the one for which the applied stress required to overcome the successive barriers is a minimum. So the application of the model requires the repetition of the calculations for all possible initiation points and crack directions, defined by the crack initiation point (angle θ) and the crack line direction (angle θ_1).

6. Predictions with the models

This section shows the notch fatigue limits predictions, σ_{FL}^N and τ_{FL}^N, with the described models for the three materials, the three types of loading and the various hole radii previously shown. The elastic stress fields to make the predictions with the models were calculated with the analytical expression of Kirsch for an infinite plate with a circular hole subjected to biaxial loading, available in elasticity books [26]. The simplification of using this analytical stress field for the studied geometry is reasonably justified, as discussed in [27]. For the MWCM+PM and Carpinteri et al. models, plane strain was assumed. Predictions with the two variants of the MWCM+PM, Mode I variant and Mode II variant, are presented. For the biaxial N-R model, the Kitawaga-Takahashi diagram was approximated with the equation proposed in [28], using f = 2.5. The number of algebraic equations was set to 200, the maximum crack length studied was set at 30 grains in length and the step of the θ and θ_1 angles for the study of the various directions was set at 1°, all with

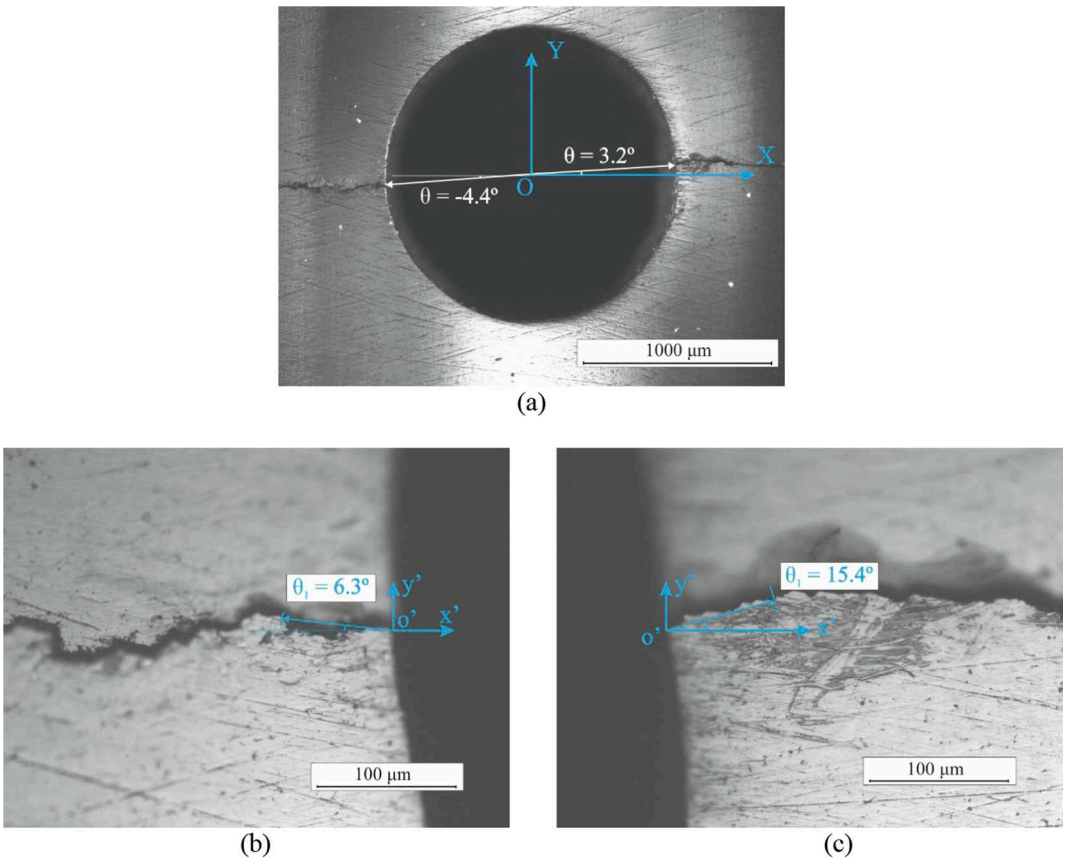

Fig. 4. Example of experimental crack angles for S355: (a) Axial loading, R = 0.75 mm, σ = 158 MPa, N = 876,500 cycles. (b) Detail of the angle θ_1 for the left crack. (c) Detail of the angle θ_1 for the right crack.

the aim of achieving a high precision in the numerical solution without an excessive computational cost.

To illustrate how the models were applied, the calculations with the various models for a specific case, material AISI 304L, $R = 0.5$ mm and axial loading, are shown below. Beginning with the MWCM+PM model, Mode I variant, the hot-spot is for this case at $\theta = 0°$ and the crack direction at $\theta_1 = 0°$. The stresses in the point located at the chosen line and at a distance of $a_0/2 = 0.09$ mm from the hot-spot, according to Kirsch's expression, for an applied axial load of 1 MPa are as follows: $\sigma_{rr} = 0.3036$ MPa, $\sigma_{\theta\theta} = 2.1328$ MPa and $\tau_{r\theta} = 0$ MPa. For this point, making simple calculations with the stress tensor, the maximum shear stress $\tau_a = 0.9146$ MPa and its corresponding normal stress $\sigma_{n,max} = 1.2182$ MPa, are calculated. These stresses when introduced in the criterion (Eq. (1)) give the prediction $\sigma_{FL}^N = 125.6$ MPa. For the Mode II variant of the MWCM+PM model, the crack direction changes to $\theta_1 = -45°$. The stresses at $a_0/2$ are in this case: $\sigma_{rr} = 0.2561$ MPa, $\sigma_{\theta\theta} = 2.2588$ MPa and $\tau_{r\theta} = 0.0828$ MPa, only slightly different from those of the Mode I variant. The stresses for the criterion are $\tau_a = 1.0048$ MPa and $\sigma_{n,max} = 1.2575$ MPa, giving the prediction $\sigma_{FL}^N = 124.7$ MPa. Regarding the model of Carpinteri et al., $\theta = 0°$ as in the previous model, while θ_1 is calculated from the angle δ. Using Eq. (2) for this material, $\delta = 0.1995$ rad $= 11.43°$ is obtained, providing $\theta_1 = -11.43°$. Again, the stresses at $a_0/2$ are: $\sigma_{rr} = 0.3009$ MPa, $\sigma_{\theta\theta} = 2.1403$ MPa and $\tau_{r\theta} = 0.0267$ MPa. The normal and shear stresses to the crack line in this point are, in modulus, $N = 2.0970$ MPa, $C = 0.2802$ MPa. When these stresses are introduced into the criterion (Eq. (3)), they provide the prediction $\sigma_{FL}^N = 149.1$ MPa. Regarding the biaxial N-R model, the calculated crack line for this case, the one for which the required applied stress to overcome the successive barriers is minimum, is defined by the angles $\theta = 4°$ and $\theta_1 = -25°$. In this line, the stresses of the biaxial N-R model at the first barrier, for an applied axial load of 1 MPa, are $\sigma_3^1 = 10.77$ MPa, $\tau_3^1 = 3.25$ MPa. For this material, the criterion parameters for the first barrier are $m_{\sigma 1}^* \cdot \tau_c = 1547$ MPa and $m_{\tau 1}^* \cdot \tau_c = 2240$ MPa. If these stresses are introduced in Eq. (4), the applied axial stress required to overcome the first barrier is 118.82 MPa. The applied stresses required to overcome the following three barriers are 138.93 MPa, 145.04 MPa and 145.02 MPa, respectively. According to previous studies, the first local maximum is the global maximum [29]. Then, the predicted fatigue limit is calculated with the third barrier and the prediction is $\sigma_{FL}^N = 145.04$ MPa.

Table 2 shows the predictions of the notch fatigue limits for the 15 studied cases. Besides, an average error for each model is presented. The fatigue limit prediction error was calculated as follows:

$$\text{Error} = \frac{\text{Prediction-Experimental}}{\text{Experimental}} \cdot 100\ (\%) \tag{5}$$

The absolute value of the errors was used to calculate the average error in order to prevent the positive and negative errors from compensating one another. In general, the models provide predictions close to the experimental ones, with an average error of less than 20% for all the models, which is considered a reasonable error in fatigue [3,1]. The smallest average error occurs for the Carpinteri et al. model, 12.1%. The other models give a very similar average error: 17.5%, 18.1% and 18.7%, for the MWCM+PM Mode I, MWCM+PM Mode II and biaxial N-R, respectively. In the case of the biaxial N-R model, the barrier that defined the notch fatigue limit was almost always within the first 10 grains.

Regarding the crack line used in the models, Table 3 includes the crack lines angles θ and θ_1 used by the models to make the predictions. The MWCM+PM and Carpinteri et al. models use the angle $\theta = 0°$ for axial load, $\theta = 45°$ for torsional load and $\theta = 31.7°$ for biaxial load, i.e the point of maximum principal stress at the hole contour, which are

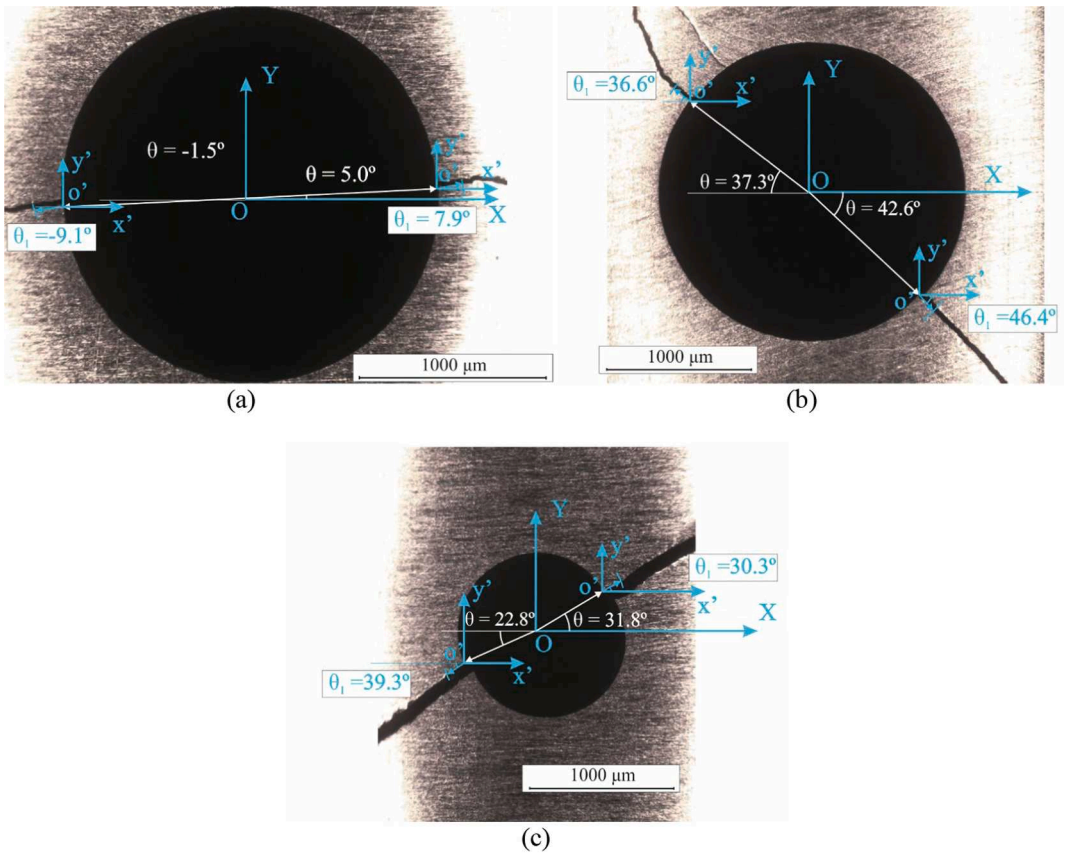

Fig. 5. Examples of experimental crack angles for 7075-T6: (a) Axial loading, R = 1 mm, σ = 110 MPa, N = 139,300 cycles. (b) Torsional loading, R = 1 mm, τ = 80 MPa, N = 788,700 cycles. (c) Biaxial loading, R = 1 mm, σ = τ = 80 MPa, N = 130,400 cycles.

Table 3
Average experimental crack angles and crack lines angles used by the models.

Material	*R*, hole radius (mm)	Type of loading	Average experimental angles		Angles used by the models							
					MWCM+PM (Mode I)		MWCM+PM (Mode II)		Carpinteri et al.		Biaxial N-R	
			θ	θ_1	θ	θ_1	θ	θ_1	θ	θ_1	θ	θ_1
AISI 304L	0.5	Axial	−0.3° (12.5°)	4.4° (8.5°)	0.0°	0.0°	0.0°	45.0°	0.0°	11.4°	4.0°	−25.0°
	1	Axial	1.3° (9.8°)	1.3° (3.8°)	0.0°	0.0°	0.0°	45.0°	0.0°	11.4°	2.0°	−20.0°
	1.5	Axial	0.9° (4.6°)	0.9° (7.8°)	0.0°	0.0°	0.0°	45.0°	0.0°	11.4°	1.0°	−17.0°
	0.5	Torsion	46.8° (6.7°)	45.2° (2.1°)	45.0°	45.0°	45.0°	0.0°	45.0°	33.6°	45.0°	−7.0°
	1	Torsion	45.9° (6.3°)	42.2° (2.8°)	45.0°	45.0°	45.0°	0.0°	45.0°	33.6°	45.0°	16.0°
	0.5	Biaxial	29.0° (4.4°)	32.0° (3.1°)	31.7°	31.7°	31.7°	−13.3°	31.7°	20.3°	35.0°	−6.0°
S355	0.4	Axial	0.3° (7.5°)	−1.0° (14.1°)	0.0°	0.0°	0.0°	45.0°	0.0°	28.7°	9.0°	−42.0°
	0.75	Axial	0.4° (4.5°)	0.4° (13.3°)	0.0°	0.0°	0.0°	45.0°	0.0°	28.7°	4.0°	−35.0°
	1.7	Axial	−0.5° (4.2°)	−5.1° (7.8°)	0.0°	0.0°	0.0°	45.0°	0.0°	28.7°	1.0°	−30.0°
7075-T6	0.5	Axial	−1.5° (8.5°)	1.2° (18.8°)	0.0°	0.0°	0.0°	45.0°	0.0°	45.0°	5.0°	−29.0°
	1	Axial	−1.1° (7.9°)	−0.4° (15.8°)	0.0°	0.0°	0.0°	45.0°	0.0°	45.0°	2.0°	−32.0°
	1.5	Axial	−0.1° (10.2°)	2.4° (19.5°)	0.0°	0.0°	0.0°	45.0°	0.0°	45.0°	1.0°	−33.0°
	0.5	Torsion	42.4° (10.4°)	47.4° (7.2°)	45.0°	45.0°	45.0°	0.0°	45.0°	0.0°	45.0°	−7.0°
	1	Torsion	45.2° (8.0°)	48.3° (11°)	45.0°	45.0°	45.0°	0.0°	45.0°	0.0°	45.0°	11.0°
	0.5	Biaxial	29.2° (7.6°)	36.6° (5.4°)	31.7°	31.7°	31.7°	−13.3°	31.7°	−13.3°	38.0°	4.0°

very close to the average experimental values also shown in Table 3. For the biaxial N-R model, the values of the angles θ used to make the predictions, obtained by scanning directions, are also close to the experimental values for all the studied cases. Regarding the angle θ_1, the MWCM+PM (Mode I variant) uses the Mode I direction, i.e $\theta_1 = 0°$ for axial load, $\theta_1 = 45°$ for torsional load and $\theta_1 = 31.7°$ for biaxial load, which are close to the average experimental values. However, the MWCM+PM (Mode II variant) uses the Mode II direction, i.e $\theta_1 = 45°$ for axial load, $\theta_1 = 0°$ for torsional load and $\theta_1 = -13.3°$ for biaxial load, which are clearly far away from the average experimental values. In the case of the Carpinteri et al. model, the angle θ_1 depends on the material, being relatively close to the experimental values for AISI 304L, further away for S355 and quite far away for Al 7075-T6, since for this last material the Mode II direction is used. For the biaxial N-R model, an intermediate value between the direction of Mode I and Mode II is generally obtained, and therefore far from the experimental values, which are close to that of Mode I. In summary, the MWCM+PM (Mode I variant) uses a crack line that is very similar to the experimental crack line, which is not the case for the rest of the models.

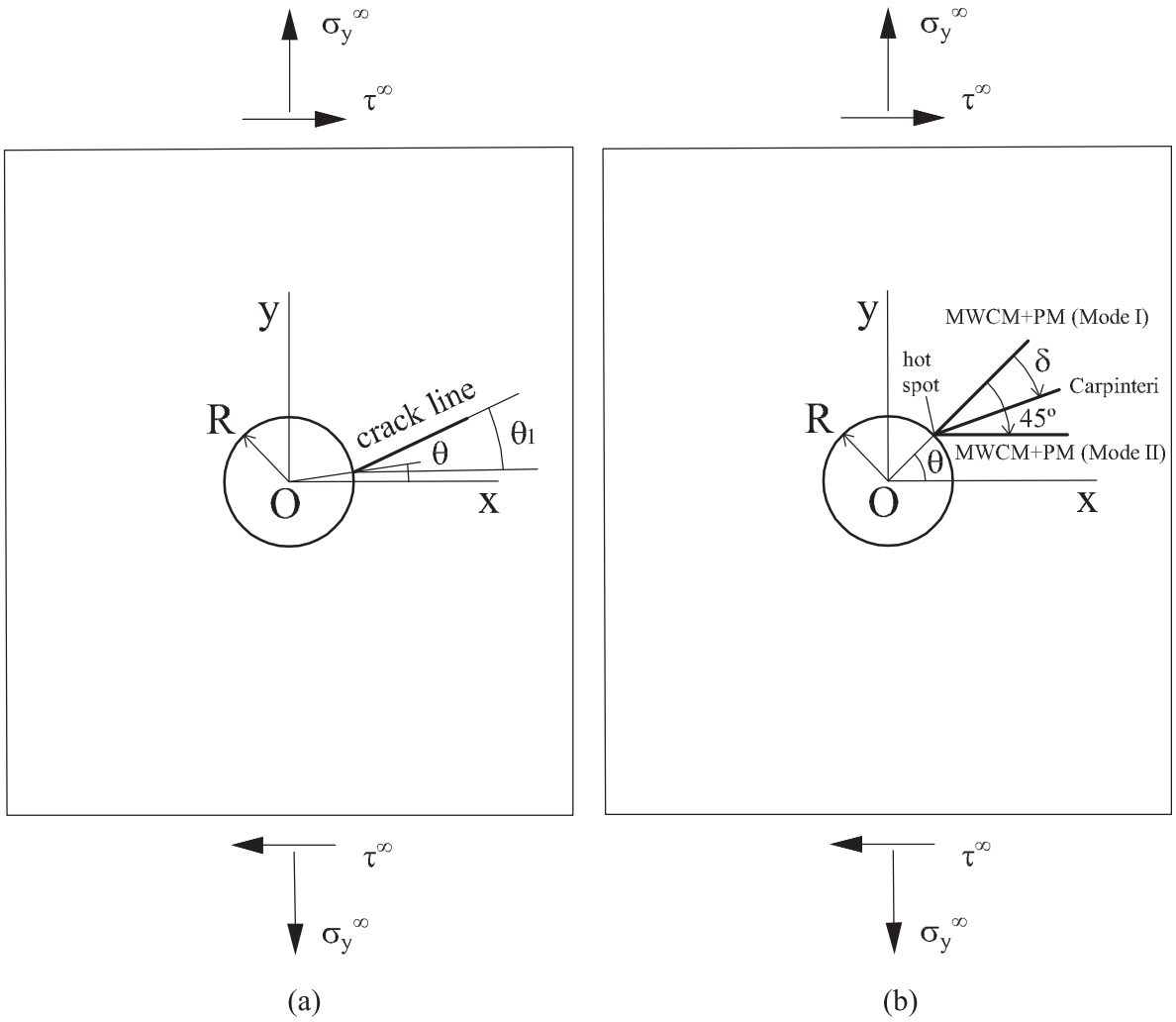

Fig. 6. Sketch of the crack lines used in the models: (a) MWCM+PM (Mode I and Mode II variant) and Carpinteri et al., (b) Biaxial N-R model.

7. Predictions with the models using the experimental crack direction

An interesting exercise is to carry out the models' predictions imposing the crack direction measured experimentally, i.e using in the models the experimental angles θ and θ_1, which in the studied cases have turned out to be, on average, close to the point of maximum principal stress and to the Mode I direction, respectively. This allows us to analyze whether the models could in the future be easily adapted to using the experimental crack direction to make the predictions.

Table 4 shows a comparison of the models' average errors using theoretical and average experimental angles θ and θ_1. The results are differentiated for the three materials. Note that when using the experimental angles, the two variants of the MWCM+PM model merge into one. As previously explained, the theoretical θ angles of all the studied models are very similar to each other, and very similar to the experimental ones, all of them are equal or close to the angle defined by the hot-spot. However, the theoretical θ_1 angles of the models present great differences among them, varying between the direction of Mode I and Mode II.

As seen in Table 4, the average errors of the MWCM+PM model using the average experimental angles are practically the same for the three materials as those obtained with the MWCM+PM model (Mode I) using the theoretical angles. It is reasonable, since as previously mentioned, the average experimental angles were very close to the Mode I direction for the studied cases. Furthermore, these errors are not far to those obtained with the MWCM+PM model (Mode II) using the theoretical angles. This result was not expected given that the average experimental angles were very far from the Mode II direction. This indicates that the MWCM+PM model is very insensitive to the angle θ_1 used for the predictions. The reason is that the stresses used in the model criterion, the maximum shear stress amplitude τ_a and its normal stress $\sigma_{n,max}$, change

Table 4
Comparison of models' errors using theoretical and average experimental angles θ and θ_1.

Material	Average error using the theoretical crack angles (%)				Average error using the average experimental crack angles (%)		
	MWCM+PM (Mode I)	MWCM+PM (Mode II)	Carpinteri et al.	Biaxial N-R	MWCM+PM	Carpinteri et al.	Biaxial N-R
AISI 304L	23.4	25.2	14.3	17.8	23.4	14.7	14.3
S355	26.7	29.3	23.2	22.3	26.7	25.2	5.7
7075-T6	8.3	6.1	5.2	20.4	8.3	6.5	175.7
Total average error (%):	18.0	18.4	12.4	19.8	18.0	13.5	77.1

very little if the angle θ_1 is varied from the Mode I to the Mode II direction, at least for this geometry, loads and materials. Regarding the model of Carpinteri et al. there is also little difference in the predictions, and therefore in the errors, when using the average experimental direction or the theoretical direction. In this case, the variation of θ_1 does cause considerable changes in the values of the criterion stresses, N and C (normal and shear stresses to the crack line). Generally, there is an increase in one of the stresses and a decrease in the another, but when introducing them into the criterion, the increase in one of them is offset by the decrease in the other, giving rise to a similar prediction. As an example, the case of material S355, $R = 1$ mm and axial load (1 MPa), with $\theta = 0^\circ$ (hot-spot) and θ_1 varying from 0° (Mode I) to 45° (Mode II) is analyzed. The stresses of the MWCM+PM model are $\tau_a = 1.18$ MPa, $\sigma_{n,max} = 1.36$ MPa for $\theta_1 = 0^\circ$ and $\tau_a = 1.25$ MPa, $\sigma_{n,max} = 1.39$ MPa for $\theta_1 = 45^\circ$, which when introduced in the criteria give the predictions $\sigma_{FL}^N = 107.6$ MPa and $\sigma_{FL}^N = 103.8$ MPa, respectively. That is, for this model the stresses and the predictions are very similar using the Mode I and Mode II directions. For the Carpinteri et al. model, the stresses are $N = 2.53$ MPa, $C = 0$ MPa for $\theta_1 = 0^\circ$ and $N = 1.54$ MPa, $C = 1.24$ MPa for $\theta_1 = 45^\circ$, which give the predictions $\sigma_{FL}^N = 108.5$ MPa and $\sigma_{FL}^N = 122.4$ MPa, respectively. In this case the stresses are very different for Mode I and Mode II directions, but the predictions are quite close, although not as much as for the MWCM+PM model.

Regarding the biaxial N-R model, as seen in Table 4, the average errors for the AISI 304L and S355 materials with the average experimental angles are even smaller than those with the theoretical angles. However, for 7075-T6, the errors using the average experimental directions are extremely large. As it happens with the Carpinteri et al. model, the criterion stresses, in this case σ_3^i and τ_3^i, change considerably as the angle θ_1 varies, so that generally one of them increases while the other decreases. The materials AISI 304L and S355, with brittle and intermediate ductile-brittle behavior, respectively, have values of the criterion parameters, $m_{\sigma i}^* \cdot \tau_c$ and $m_{\tau i}^* \cdot \tau_c$, of the same order of magnitude, so the increase of one of the stresses is partially compensated by the decrease of the other when they are introduced into the criterion, giving rise to predictions that are not very different. However, for the material 7075-T6, considered to be brittle in fatigue, the parameters $m_{\sigma i}^* \cdot \tau_c$ and $m_{\tau i}^* \cdot \tau_c$ have a very different magnitude. So the changes of the stresses σ_3^i and τ_3^i with the variation of θ_1 are not compensated in any way when introduced into the criterion, giving rise to very different predictions. Let́s analyze again the example of $R = 1$ mm and axial load (1 MPa), with $\theta = 0^\circ$ (hot-spot) and θ_1 varying from 0° (Mode I) to 45° (Mode II). For the material S355, the stresses of the biaxial N-R model at the first barrier are $\sigma_3^1 = 14.3$ MPa, $\tau_3^1 = 0$ MPa for $\theta_1 = 0^\circ$ and $\sigma_3^1 = 9.0$ MPa, $\tau_3^1 = 4.7$ MPa for $\theta_1 = 45^\circ$. For this material, the criterion parameters for the first barrier are $m_{\sigma 1}^* \cdot \tau_c = 1785$ MPa and $m_{\tau 1}^* \cdot \tau_c = 1076$ MPa. Assuming for simplicity that the fatigue limit is obtained with the first barrier, the predictions would be $\sigma_{FL}^N = 125.3$ MPa and $\sigma_{FL}^N = 105.6$ MPa, respectively, that is, not very different from each other. If the same analysis is done for material 7075-T6, the stresses of the model are $\sigma_3^1 = 14.5$ MPa, $\tau_3^1 = 0$ MPa for $\theta_1 = 0^\circ$ and $\sigma_3^1 = 9.1$ MPa, $\tau_3^1 = 4.8$ MPa for $\theta_1 = 45^\circ$, that is, quite similar to those obtained for the material S355. However, the criterion parameters for the first barrier are now $m_{\sigma 1}^* \cdot \tau_c = 4247$ MPa and $m_{\tau 1}^* \cdot \tau_c = 666$ MPa, that is, quite different in magnitude. The predictions would be now $\sigma_{FL}^N = 292.3$ MPa and $\sigma_{FL}^N = 106.5$ MPa, respectively, which means that difference between both predictions is extremely large. In summary, although the biaxial N-R predictions with the average experimental directions are the best for AISI 304L and S355, they turn out to be unacceptable for Al 7075-T6.

7.1. Analysis of the effect on the predictions of the experimental angles' standard deviations

As seen in Table 3, the average experimental angles θ are close to those defined with the hot-spot and θ_1 are close to Mode I direction. But the dispersion of these values are relatively large for all the materials, hole radii and loading, as seen in the standard deviation of these values, shown in parentheses in Table 3. This dispersion in the experimental crack angles is reasonable, since for the tested specimens there is obviously a dispersion in the surface finish quality at the notch surface and in the material microstructure (distribution of grains, pores, inclusions, etc.), which has an influence on where the crack initiates and in which direction, especially in high cycle fatigue. This section shows an analysis of the effect of this dispersion on the models' predictions calculated with the experimental angles. Starting from the average experimental angles θ and θ_1, whose predictions are called $\sigma_{FL}^N(\exp(\theta, \theta_1))$, a sweep of θ and θ_1 angles of ± 1 standard deviation s of each of the variables was performed. The model's predictions were made for all these directions, providing a range of predictions $\left(\sigma_{FL}^N(\max), \sigma_{FL}^N(\min)\right)$. Their dimensionless values, expressed as a percentage, were calculated using the following expressions:

$$\sigma_{FL}^N(\max,\ \dim) = \frac{\sigma_{FL}^N(\max) - \sigma_{FL}^N(\exp(\theta, \theta_1))}{\sigma_{FL}^N(\exp(\theta, \theta_1))} \cdot 100 \tag{6}$$

$$\sigma_{FL}^N(\min, \dim) = \frac{\sigma_{FL}^N(\min) - \sigma_{FL}^N(\exp(\theta, \theta_1))}{\sigma_{FL}^N(\exp(\theta, \theta_1))} \cdot 100 \tag{7}$$

Note that Eq. (6) will always provide a positive value while Eq. (7) will always provide a negative value. Table 5 shows the average of these values for each material and model. Besides, a total average for each model is shown. As expected, after the analysis in the previous section, the dispersion of θ and θ_1 experimental angles generates very low dispersion in the MWCM+PM's predictions for the three materials, and a bit more dispersion in the Carpinteri et al.'s predictions. Regarding the biaxial N-R model, there is a clear effect of the material, generating low dispersion for the AISI 304L, a higher dispersion for the S355 and a very high dispersion for the 7075-T6. These results indicate that the MWCM+PM's and Carpinteri et al.'s predictions using the average experimental angles are highly representative of these models' predictions for the entire range of experimental angles. The same is not the case with the biaxial N-R model, especially for the 7075-T6 material, for which it would be convenient to give a range of predictions and not just the value for the average experimental angles.

8. Discussion

The experimental results shown in this work indicate that the fatigue crack initiates from a point of the notch contour close to the hot-spot and grows in its initial part close to the Mode I direction. These results were obtained after analyzing 106 specimens of three materials, with several hole radii and three types of loading, in the high cycle fatigue regime. This is a large study, although it is not comprehensive. Regarding the hole radii, values around 1 mm were analyzed, missing the study of very small radii, of the order of grain size, and very large radii, of the order of several mm. Recently, Lorenzino and Navarro tested an aluminum alloy with very large grains [15]. The specimens had a circular hole whose radius was of the order of the grain size and were subjected to cyclic axial loading. They observed a great dispersion of the crack initiation point and very irregular crack paths in their initial part, greatly affected

Table 5
Range of predictions using the average experimental angles θ and θ_1 ± 1 s.

Material	Range of predictions: $\left(\sigma_{FL}^N(\max,\ \dim), \sigma_{FL}^N(\min,\ \dim)\right)$(%)		
	MWCM+PM	Carpinteri et al.	Biaxial N-R
AISI 304L	(3.5, −0.2)	(4.8, −0.1)	(1.8, −4.0)
S355	(1.5, −0.6)	(1.6, 0.0)	(3.1, −15.9)
7075-T6	(4.8, −0.6)	(4.6, −3.1)	(25.9, −46.6)
Total average:	**(3.6, −0.4)**	**(4.1, −1.3)**	**(11.7, –23.4)**

by the microstructure of the material. From which it can be deduced that the main conclusions of the experimental results shown in the present work should not be extrapolated to very small holes as compared to the microstructure, expecting for these cases a great dispersion on the crack initiation direction. Regarding very large holes, according to our knowledge there are no crack initiation direction studies in the literature on this size. The effect of the microstructure would be expected to be less than for small holes and therefore the crack would initiate close to the hot-spot and grow in its initial part close to the Mode I direction, with lower dispersion in the crack initiation direction. Regarding the type of notch, the present study was focused on circular notches, with a K_t value of approximately 3. It would be very interesting to complete the present study in the future with the analysis of other notch geometries, such as V-notches, with K_t values higher and lower than 3. With respect to the type of loading, the most common load cases were studied, such as axial, torsional and in-phase biaxial. The study of the mean stress and the out-of-phase effects would be enriching. Regarding the studied materials, three materials were tested: a stainless steel, a carbon steel and an aluminum alloy, considered as brittle, intermediate ductile-brittle and ductile in fatigue. Therefore, regarding the ductility of materials the present work can be considered as very complete. No significant differences were observed in the crack direction in its initial part for the three materials. An initial direction in Mode II for the ductile material was not observed, that is, for all materials the direction was that of Mode I. Forsyth literally said in his fatigue book [30]: "…it has been observed that this slip-band crack growth commonly changes to normal growth when the tip of the crack reaches the first grain boundary…". According to this statement, a Mode II initiation at the first grain could have occurred in the studied materials, but it would not have been observed in the present study, where cracks of, at least, several grains in length were analyzed. It would be interesting for the future to carry out a study of experimental crack directions in the first grain for notches and verify if the Mode II direction prevails.

An important parameter of the present study is the crack length a used to measure the experimental crack direction angle θ_1. It was set to 0.50, 0.08 and 0.15 mm for the AISI 304L, S355 and 7075-T6 specimens, respectively, that is, a different length for each material. These lengths are also different if they are expressed as a function of the El Haddad length a_0, being $2.8a_0$, $0.5a_0$, and $2.1a_0$, respectively, or, as a function of the average grain size, 6.2d, 2.4d and 10d, respectively. The reason for choosing these lengths is explained below. For the AISI 304L, chronologically the first tested material, a length that was of the order of 5–10 grains and of the order of a_0 was sought, so that it would be representative of the typical lengths used for the predictions with the N-R model and the TCD ($a_0/2$ for the point method and $2a_0$ for the line method), respectively. In addition, the length should not be too small, in order to make possible an optical analysis of the crack. The chosen length was 0.50 mm, equivalent to 6.2 grains and $2.8a_0$. The second studied material was the 7075-T6. This material had a very small grain, 0.015 mm, so it was decided to choose the largest possible length without exceeding 10 grains. So, a length of 0.150 mm was chosen, equivalent to 10 grains and $2.1a_0$. For the third studied material, the S355, a length of $a_0/2$ was chosen, as the chosen lengths for the two previous materials were clearly larger than $a_0/2$, length used in the point method. The length was 0.08 mm, equivalent to 2.4 grains. The study done on S355 steel included experimental angles θ_1 measured at various lengths, such as $0.5a_0$, a_0, and $2a_0$, in order to analyze the influence of this length in the measured angles θ_1. The average θ_1 angles were very similar for these three lengths. For example, for the radius $R = 0.4$ mm, the average θ_1 angles were $-1.0°$, $-2.9°$ and $0.8°$ for lengths $0.5a_0$, a_0, and $2a_0$, respectively. This indicates that for this material the average crack direction changes little for crack lengths of the order of a_0. Based on these results, the average measured angles θ_1 shown in this work, measured for the lengths defined above for the three studied materials, were considered representative of the crack direction in its initial part, which is the part of the crack that the studied models are supposed to use for their predictions.

Regarding the analyzed models, used for the prediction of the notch fatigue limit under biaxial loading, they provided in general good predictions for the studied cases. In addition, the application of the models using, in a forced way, the experimental crack direction to make the predictions were also good (with the exception of the biaxial N-R model applied to the 7075-T6 material). These results allow us to glimpse that in the near future the models could use directions close to the experimental ones for the predictions, so that both the numerical predictions of the fatigue limits and the directions used were close to the experimental measurements. Although previously it will be necessary to extend the experimental work of the type shown in the present document to more geometries, loads, etc. In our opinion, this would result in a higher quality of the models, which would increase the confidence of the industry in them.

9. Conclusions

In this work an analysis of the fatigue limits in notched specimens under biaxial cyclic loading was shown, including the experimental results for specimens with several hole sizes, three materials and three types of loading, and the experimental predictions with three models. Two of the models were based on a combination of the Critical Plane Approach with the Theory of Critical Distances and the third was a short crack microstructural model. Regarding the experimental work, the crack directions of 106 notched specimens were analyzed. The most remarkable thing is that for the three studied materials and the three types of loading the crack initiation point was approximately that of maximum principal stress at the notch contour and the crack direction in its initial part was close to that of Mode I, despite the fact that the three materials were very different in terms of their ductility, being one of the ductile type, another semi-ductile and the other brittle. Regarding the models, they generally gave good predictions, even if the use of the experimental crack direction was imposed to make the predictions. This last conclusion opens the possibility for the models to unify the crack lines used for the predictions, based on the experimental ones, which would make them closer to the experimental reality, and therefore more reliable.

CRediT authorship contribution statement

V. Chaves: Conceptualization, Methodology, Software. **J.A. Balbín:** Investigation. **A. Navarro:** Conceptualization, Visualization, Investigation. **L. Susmel:** Conceptualization, Supervision. **D. Taylor:** Conceptualization, Supervision.

Declaration of Competing Interest

The authors declare that they have no known competing financial interests or personal relationships that could have appeared to influence the work reported in this paper.

Data availability

Data will be made available on request.

Acknowledgements

The authors would like to thank the European Union, the Spanish Government and the Junta de Andalucía, Spain, for its financial support through grants PID2020-117407GB-I00 (FEDER/Ministerio de Ciencia e Innovación - Agencia Estatal de Investigación) and P18-FR-4306 ("Fondo Europeo de Desarrollo Regional (FEDER) y Consejería de Economía, Conocimiento, Empresas y Universidad de la Junta de Andalucía, dentro del Programa Operativo FEDER 2014–2020'').

References

[1] Susmel L. Multiaxial notch fatigue: from nominal to local stress/strain quantities. Woodhead Publishing; 2009.
[2] Carpinteri A, Spagnoli A, Vantadori S, Viappani D. A multiaxial criterion for notch high cycle fatigue using a critical-point method. Eng Fract Mech 2008;75:1864–74.
[3] Taylor D. The theory of critical distances: a new perspective in fracture mechanics. Elsevier; 2007.
[4] Chaves V, Navarro A, Beretta G, Madrigal C. Microstructural model for predicting high cycle fatigue strength in the presence of holes under proportional biaxial loading. Theor Appl Fract Mec 2014;73:27–38.
[5] El Haddad MH, Topper TH, Smith KN. Prediction of non propagating cracks. Eng Fract Mech 1979;11(3):573–84.
[6] Fenner AJ, Owen NB, Phillips CE. A note on the fatigue crack regarded as a stress raiser. Engineering 1951;171:637–8.
[7] Frost NE. Notch effect and the critical alternating stress required to propagate a crack in an aluminium alloy subject to fatigue loading. J Mech Eng Sci 1960;2(2):109–19.
[8] Kitagawa H, Takahashi S. Applicability of fracture mechanics to very small cracks or the cracks in the early stages. In: Second International Conference on Mechanical Behavior of Materials, American Society for Metals, Cleveland, 1976.
[9] Endo M. The multiaxial fatigue strength of specimens containing small defects, in: Biaxial/multiaxial fatigue and fracture ESIS publication 2003; Vol. 31 : 243–264.
[10] Susmel L, Taylor D. Non-propagating cracks and high-cycle fatigue failures in sharply notched specimens under in-phase Mode I and II loading. Eng Fail Anal 2007;14(5):861–76.
[11] Meneghetti G, Susmel L, Tovo R. High-cycle fatigue crack paths in specimens having diferent stress concentration features. Eng Fail Anal 2007;14(4):656–72.
[12] Tanaka K, Morita K, Akinawa Y. Fatigue thresholds of holed components under in-phase and out-of-phase torsional and axial loadings. Fatigue Fract Eng Mater Struct 2008;31(12):1079–90.
[13] Berto F, Lazzarin P, Yates JR. Multiaxial fatigue of v-notched steel specimens: a non-conventional application of the local energy method. Fatigue Fract Eng Mater Struct 2011;34(11):921–43.
[14] Gates N, Fatemi A. Notched fatigue behavior and stress analysis under multiaxial states of stress. Int J Fatigue 2014;67:2–14.
[15] Lorenzino P, Navarro A. Growth of very long “short cracks” initiated at holes. Int J Fatigue 2015;71:64–74.
[16] Chaves V, Beretta G, Navarro A. Biaxial fatigue limits and crack directions for stainless steel specimens with circular holes. Eng Fract Mech 2017;174:139–54.
[17] Balbín JA, Chaves V, Larrosa NO, Madrigal C, Navarro A. Directions of high cycle fatigue cracks emanating from circular notches studied by optical profilometry. Int J fatigue 2022;165:107117.
[18] Chaves V, Beretta G, Balbin JA, Navarro A. Fatigue life and crack growth direction in 7075–T6 aluminium alloy specimens with a circular hole under biaxial loading. Int J fatigue 2019;125:222–36.
[19] Gough HJ, Pollard HV, Clenshaw WJ. Some experiments on the resistance of metals to fatigue under combined stresses. In: Ministry of Supply, Aeronautical Research Council Reports and Memoranda. London: His Majesty’s Stationary Office; 1951. p. 1–141.
[20] Chaves V, Navarro A, Madrigal C, Vallellano C. Calculating crack initiation directions for in-phase biaxial fatigue loading. Int J Fatigue 2014;58:166–71.
[21] Navarro A, Vallellano C, de los Rios ER, Xin XJ. Notch sensitivity and size effects by a short crack propagation model. In: Engineering Against Fatigue, Proc Int Conf. Rotterdam: AA Balkema Publishers; 1997, Sheffield, 1999.
[22] Susmel L. A unifying approach to estimate the high-cycle fatigue strength of notched components subjected to both uniaxial and multiaxial cyclic loadings. Fatigue Fract Engng Mater Struct 2004;27(5):391–411.
[23] Taylor D. Notch sizze effect in multiaxial fatigue, in: Progettazione a fatica in presenza di multiassialitá tensionali. L. Susmel, R. Tovo, editors; Ferrara,2005.
[24] Navarro A, de los Rios ER. Short and long fatigue crack growth: a unified model. Philos Mag A 1988;57:12–36.
[25] Navarro A, de los Rios ER. An alternative model of the blocking of dislocations at grain boundaries. Philos Mag A 1988;57:37–42.
[26] Timoshenko S, Goodier JN. Theory of Elasticity. McGraw-Hill; 1934.
[27] Chaves V, Navarro A, Susmel L, Taylor D. Analysis of biaxial fatigue limit models for cases with circular notches. Int J Fatigue 2022;162:106981.
[28] Vallellano C, Navarro A, Dominguez J. Fatigue crack growth threshold conditions at notches. Part I: theory. Fatigue Fract Eng Mater Struct 2000;23:113–21.
[29] Chaves V, Madrigal C, Navarro A. Fatigue limit predictions at stress concentrations using FEA and microstructural fracture mechanics. Theor Appl Fract Mech 2017;87:11–20.
[30] Forsyth PJE. The physical basis of metal fatigue. Glasgow: Blackie and son limited; 1969.